# Comparison of Modeled and Measured Ice Nucleating Particle Composition in a Cirrus Cloud

ROMY ULLRICH,[a] CORINNA HOOSE,[a] DANIEL J. CZICZO,[b] KARL D. FROYD,[c] JOSHUA P. SCHWARZ,[c] ANNE E. PERRING,[c] THAOPAUL V. BUI,[d] CARL G. SCHMITT,[e] BERNHARD VOGEL,[a] DANIEL RIEGER,[a,f] THOMAS LEISNER,[a] AND OTTMAR MÖHLER[a]

[a] *Institute of Meteorology and Climate Research, Karlsruhe Institute of Technology, Karlsruhe, Germany*
[b] *Department of Earth, Atmospheric and Planetary Sciences, and Department of Civil and Environmental Engineering, Massachusetts Institute of Technology, Cambridge, Massachusetts*
[c] *NOAA/Earth System Research Laboratory/Chemical Sciences Division, Boulder, Colorado*
[d] *Atmospheric Science Branch, NASA Ames Research Center, Mountain View, California*
[e] *Dynamical and Physical Meteorology, Mesoscale and Microscale Meteorology Laboratory, NCAR, Boulder, Colorado*

(Manuscript received 29 January 2018, in final form 18 January 2019)

ABSTRACT

The contribution of heterogeneous ice nucleation to the formation of cirrus cloud ice crystals is still not well quantified. This results in large uncertainties when predicting cirrus radiative effects and their role in Earth's climate system. The goal of this case study is to simulate the composition, and thus activation conditions, of ice nucleating particles (INPs) to evaluate their contribution to heterogeneous cirrus ice formation in relation to homogeneous ice nucleation. For this, the regional model COSMO—Aerosols and Reactive Trace Gases (COSMO-ART) was used to simulate a synoptic cirrus cloud over Texas on 13 April 2011. The simulated INP composition was then compared to measured ice residual particle (IRP) composition from the actual event obtained during the NASA Midlatitude Airborne Cirrus Properties Experiment (MACPEX) aircraft campaign. These IRP measurements indicated that the dominance of heterogeneous ice nucleation was mainly driven by mineral dust with contributions from a variety of other particle types. Applying realistic activation thresholds and concentrations of airborne transported mineral dust and biomass-burning particles, the model implementing the heterogeneous ice nucleation parameterization scheme of Ullrich et al. is able to reproduce the overall dominating ice formation mechanism in contrast to the model simulation with the scheme of Phillips et al. However, the model showed flaws in reproducing the IRP composition.

## 1. Introduction

Cirrus clouds are ice clouds existing in the upper troposphere (Kärcher and Spichtinger 2009; Heymsfield et al. 2017). Because of their wide range of optical thickness (Heymsfield et al. 2017), cirrus clouds feature a diverse radiative effect (Kärcher and Spichtinger 2009; Boucher et al. 2013) and therefore, their role in the climate system is still not well resolved. To quantify the cirrus radiative effect, Krämer et al. (2016) and Luebke et al. (2013) recently classified cirrus clouds according to their formation process and resulting microphysical properties (e.g., ice water content, optical thickness, or ice particle size). Those authors propose two main classes of cirrus clouds: 1) in situ–origin cirrus and 2) liquid-origin cirrus. The latter type defines glaciated mixed-phase clouds with high optical thickness and many large ice particles (Krämer et al. 2016). In other studies this type of clouds was named convective or anvil cirrus (e.g., Lynch et al. 2002). In contrast, ice in situ–origin cirrus is formed directly from the vapor phase in cyclonic circulations, jet streams, or gravity waves (Krämer et al. 2016). This type combines the former classes of synoptic cirrus, lee wave– and gravity wave–induced, and orographic cirrus (Heymsfield et al. 2017).

The differentiation of cirrus types is directly linked to the formation mechanism of the ice particles. In liquid-origin cirrus clouds droplets freeze either homogeneously or heterogeneously when an insoluble ice

[f] Current affiliation: German Meteorological Service, Offenbach, Germany.

*Corresponding author*: Corinna Hoose, corinna.hoose@kit.edu

DOI: 10.1175/JAS-D-18-0034.1

nucleating particle (INP) is immersed in the droplet. In contrast, ice particles of in situ cirrus form either by homogeneous freezing of solution droplets or by the deposition of water vapor on INPs. The dominant formation mechanism is still unclear, but depends on the orography, updraft velocity and the INP burden (Mitchell et al. 2016; Gasparini and Lohmann 2016). Some studies (model as well as field) have found an overall dominance of homogeneous ice nucleation (e.g., Heymsfield and Miloshevich 1993; Gettelman et al. 2010). However, these studies probably overestimated the ice particle number concentration and thereby the role of homogeneous ice nucleation, because of ice crystal shattering during the measurements (Cziczo and Froyd 2014). There are also modeling studies proposing a strong contribution of heterogeneous ice nucleation. Jensen et al. (2016) compared regional model simulation with aircraft and satellite observations, and found that homogeneous ice nucleation was dominant, but also stated the need of heterogeneous ice formation for reproducing observed ice particle concentrations. The simulations of Shi et al. (2015) suggest that on a global mean less than 20% of cirrus clouds are formed by homogeneous ice nucleation. Further, field observations of ice residual particles (IRPs) indicate the importance of heterogeneous ice nucleation in both liquid origin clouds (e.g., Kamphus et al. 2010) and in situ cirrus (e.g., Cziczo et al. 2013). The diverse results of the modeling studies might be due to the different ice nucleation schemes implemented in the models (Li et al. 2012; Komurcu et al. 2014). Furthermore, the dominating ice formation mechanism predicted by models is highly sensitive to the assumed INP spectra and the implemented heterogeneous ice nucleation parameterization (Barahona et al. 2010; Sullivan et al. 2016).

Previous modeling studies on the impact of homogeneous and heterogeneous ice nucleation on cirrus cloud formation were limited to comparisons with observed ice particle concentrations and/or sizes. However, these measurements provide reliable values only for ice particles above about 100 $\mu$m (Heymsfield et al. 2017) and hence do not include small ice particles. On the other hand, the chemical composition analysis of IRPs provide direct information about the nature of INPs and are therefore suggestive of the underlying ice nucleation mechanism (Cziczo et al. 2013). In our study we aim to compare modeled INP with IRP compositions measured during the Midlatitude Airborne Cirrus Properties Experiment (MACPEX) aircraft campaign in spring 2011. For that we used the Consortium for Small-Scale Modeling (COSMO) model extended by the Aerosol and Reactive Trace Gases (ART) module described in section 2. In contrast to many previous model sensitivity studies (e.g., Zhang et al. 2013; Sullivan et al. 2016), which focused on the sensitivity of cloud properties on the INP parameterization, we apply two parameterization schemes for heterogeneous ice nucleation (Phillips et al. 2013, hereafter P13; Ullrich et al. 2017, hereafter U17) to compare modeled INPs with field observations of IRP. Section 3 describes the MACPEX aircraft campaign and the instrumentation. The model result and their comparison to observations of the ice particle concentration and the IRP composition measured by the Particle Analysis by Laser Mass Spectrometry (PALMS) instrument are presented in section 4.

## 2. COSMO-ART model

### a. Model description

The regional-scale model used in this study is the COSMO model (Baldauf et al. 2011; Doms and Baldauf 2015) with its online coupled module ART treating aerosol–trace gases–cloud interactions (Vogel et al. 2009). The COSMO model is a nonhydrostatic atmospheric prediction model operating on an Arakawa C grid with terrain-following vertical coordinates. The prognostic differential equations are solved numerically with a finite differences algorithm (third-order Runge–Kutta scheme) and a two-level time-splitting scheme (Doms and Baldauf 2015).

In the configuration used in this study, the cloud microphysics in the COSMO model uses a two-moment bulk microphysics scheme based on the work of Seifert and Beheng (2006). In this scheme six hydrometeor classes (cloud droplets, rain, cloud ice, snow, graupel, and hail) are distinguished, each represented by a generalized gamma distribution with constant shape factors. Additionally, the cloud droplet and ice crystal formation is treated as aerosol dependent. Thereby, the aerosols in ART are categorized into 11 modes with respect to their chemical composition and size (see Table 1), and are represented by lognormal size distributions with prescribed widths and prognostic mass and number concentrations (Vogel et al. 2009; Bangert et al. 2012).

Two modes of secondary mixed particles and the three modes of sea salt form solution droplets and will contribute to homogeneous freezing in the setup used in this study. Another three modes represent mineral dust. For mineral dust and sea salt, emission, transport, and removal schemes are implemented into the ART module. The emissions are parameterized as a function of

TABLE 1. Aerosol classes treated in the ART module and used in this study with their corresponding size range, chemical composition, and ice nucleation (IN) process to which they contribute. "Het" indicates heterogeneous ice nucleation and "hom" homogeneous freezing of solution droplets.

| Aerosol class | Aitken mode | Accumulation mode | Coarse mode | Chemical composition | IN process |
|---|---|---|---|---|---|
| Secondary mixed | × | × | — | $SO_4^{2-}$, $NO_3^-$, $NH_4^+$, $H_2O$, SOA | Hom |
| Internally mixed soot | × | × | — | $SO_4^{2-}$, $NO_3^-$, $NH_4^+$, $H_2O$, SOA, BC | Het |
| Soot | — | × | — | BC | Het |
| Mineral dust | — | × | × (two modes) | — | Het |
| Sea salt | — | × | × (two modes) | — | Hom |

atmospheric state and surface properties (Vogel et al. 2006; Lundgren et al. 2013). In the model, both aerosol types do not interact with other particles or gases. Soot is represented by one mode of directly emitted pure black carbon (BC) and two modes of internally mixed BC from anthropogenic and natural sources in different size ranges and contributes with all three modes to heterogeneous ice nucleation.

The recently implemented plume rise model (Walter et al. 2016) treats the emission and transportation of trace gases and aerosol from wildfires. The BC aerosol concentrations generated by this model are added online to the pure and internally mixed soot modes, which can potentially act as INP according to the parameterization described below.

The formation of cloud ice particles by homogeneous and heterogeneous ice nucleation, which compete and interact with each other on temporal and spatial scales smaller than those resolved by the model, is parameterized using the scheme of Barahona and Nenes (2009a,b). For temperatures above 235 K or if a liquid-phase cloud exists, only heterogeneous ice nucleation takes place. For temperatures below 235 K a competition between homogeneous freezing and heterogeneous ice nucleation takes place depending on the updraft velocity, relative humidity, temperature, and relative particle concentrations. The homogeneously nucleated ice particle number concentration is calculated following the scheme of Barahona and Nenes (2008) and Barahona et al. (2010). The ice number concentration of heterogeneously frozen aerosol particles entering the Barahona and Nenes (2009a,b) scheme is given by additional parameterization schemes of P13 or U17.

The aerosol particle concentration is given by the model internal emission scheme and the data initializing the model as described in section 4b. The relative humidity and the temperature at which the ice nucleation takes place strongly depends on the vertical velocity (Barahona et al. 2017). Because of the resolution of the model, a parameterization of subgrid-scale vertical velocities is needed to control the ice nucleation. The subgrid-scale vertical velocity is parameterized with a Gaussian probability distribution function (Bangert et al. 2012) depending on the resolved grid-scale vertical velocity and the subgrid turbulent kinetic energy, which is in turn a prognostic variable in the subgrid turbulence scheme, which follows Mellor and Yamada (1974) as described in Doms et al. (2011). This subgrid-scale vertical velocity distribution is then used in the ice nucleation scheme of Barahona and Nenes (2009a,b) to calculate the maximum ice saturation ratio and thus the temperature reached for ice nucleation.

### *b. Parameterization for heterogeneous ice nucleation*

To determine the INP concentration and composition, two different aerosol-specific parameterizations for heterogeneous ice nucleation are used in this study. In COSMO-ART, the scheme of Phillips et al. (2008) is generally used as a default (Bangert et al. 2012), but was updated to its latest version (P13) for our study. Additionally, we implemented and applied the parameterization for heterogeneous ice nucleation developed by U17, another aerosol-specific INP parameterization scheme, but much easier to implement than the P13 scheme. Furthermore, the U17 scheme is solely based on laboratory experiments at the Aerosol Interaction and Dynamics in the Atmosphere (AIDA) chamber at the Karlsruhe Institute of Technology (KIT), whereas the P13 scheme is based on field measurements with a continuous flow diffusion chamber (CFDC) and the Meyers et al. (1992) scheme. Both schemes provide parameterization functions for mineral dust particles and soot particles in the temperature regime of mixed-phase and cirrus clouds. A description of both schemes can be found in the appendix. For the heterogeneous ice nucleation, the three modes of the soot class were summed to calculate the total number concentration of INP, whereas the INP concentration from mineral dust is calculated independently for each mode and then summed. This implies that the soot mixing state predicted by COSMO-ART (pure and internally mixed) is not taken into

account for its ice nucleation properties of the particles. In sensitivity experiments, we will explore the maximum effect of aging.

## 3. MACPEX campaign

The NASA MACPEX campaign (Jensen et al. 2013; Rollins et al. 2014) was undertaken to determining the microphysical properties of ice crystals in midlatitude cirrus clouds, with a special focus on the occurrence and influence of small ice crystals and the influence of aerosol particles as INP in cirrus clouds. During the campaign in March and April 2011, the NASA science aircraft WB-57F was based at Ellington Field, Texas, for 14 science flights in synoptic and anvil cirrus clouds over the south-central United States. To accomplish the scientific goals of the campaign, the WB-57F payload included instruments measuring ice particle size, habit and residuals, aerosol concentration and composition, and water vapor concentration.

A single-particle mass spectrometer (SPMS) combined with a redesigned counterflow virtual impactor (CVI; Cziczo et al. 2013; Cziczo and Froyd 2014) inlet allowed for measurement of the aerosol particles composition outside and IRP composition inside the cirrus. The particles sampled by the SPMS PALMS instrument are desorbed and ionized by an excimer laser, and characterized by a time-of-flight mass spectrometer. PALMS analyzed particles with an aerodynamic diameter between 0.2 and 3.0 $\mu$m (Thomson et al. 2000; Cziczo et al. 2013). The new CVI inlet enabled the measurement of ice particles with aerodynamic diameters up to 70 $\mu$m (Cziczo and Froyd 2014). Before the IRPs can be analyzed with the PALMS instrument, the interstitial aerosol is rejected by the CVI inlet and the remaining ice particles are heated by an inline laser to about 50°C to remove water. Based on the observed positive and negative mass spectra, each particle is classified by the appearance and relative intensities of specific peaks as described by Froyd et al. (2009). The uncertainty in classification is about 1%–5% (Froyd et al. 2009). Mass spectra with indication of ice particle impaction artifacts are removed (Cziczo and Froyd 2014). Finally, to infer the predominant nucleation mechanism in the cirrus, the averaged clear-sky aerosol composition is compared with the averaged IRP composition. In the case that the IRP composition differs substantially from clear-sky aerosol composition (e.g., contains a high fraction of mineral dust), heterogeneous ice nucleation is inferred (Cziczo et al. 2013).

The NOAA single-particle soot photometer (SP2) instrument measured the mass concentration of pure BC particles as well as internally mixed BC particles in the size range of 90–600-nm volume-equivalent diameter (just for the BC component; Schwarz et al. 2006). A laser beam inside the SP2 heats BC-containing particles and evaporates nonrefractory coatings. Further laser heating causes the BC cores to emit thermal radiation in intensities that depend on the BC mass. The uncertainty in the BC mass concentration of 40% is the sum of standard deviations from flow and mass calibration, and aspiration efficiency (Schwarz et al. 2006). Further note that the lower detection limit might result in a significant number of uncounted BC-containing particles. However, these particles are not expected to contribute significantly to the total BC mass concentration. The SP2 was sampling through a flat plate inlet (Perring et al. 2013), which performed similarly to a previously evaluated forward-facing diffuser inlet in clear air, and allowed in-cloud sampling of interstitial aerosol without artifacts. Further note that the SP2 was not sampling from a CVI inlet and therefore did not measure IRP.

The ice particle size distribution and concentration was measured by several instruments. The video ice particle sampler (VIPS) collects continuously particles on a loop belt coated with silicon oil and images these particles with a video microscope (e.g., Heymsfield and Miloshevich 1995; Schmitt and Heymsfield 2009). In the case of the MACPEX campaign, particles with diameters between 10 and 200 $\mu$m were detected. Larger ice crystals and snow particles were detected with the high-volume precipitation spectrometer (HVPS) and the two-dimensional stereo (2D-S) probe. The 2D-S probe uses two orthogonal laser beams to image the two-dimensional shadow of the particles passing the cross section (Lawson et al. 2006). From the shadows, particle size and habit are determined following the algorithm described in Lawson (2011). Thereby, biased number concentrations of small particles due to shattering are removed (Lawson 2011). The HVPS uses the same mechanism but with a larger detection volume to detect larger particles. Therefore, combined measurements of 2D-S and HVPS can probe particles with diameters from 10 $\mu$m to about 3 mm and from 300 $\mu$m up to about 2 cm [from the measurement data sheets available from NASA (2012)]. Note that all three measurement techniques give maximum dimension diameters (e.g., McFarquhar and Heymsfield 1996). The estimation of uncertainties in sizing and counting of the particles is still an ongoing task. Some uncertainties are discussed in Lawson et al. (2008), Schmitt and Heymsfield (2009), and Lawson (2011).

The atmospheric state parameters pressure, temperature, wind vector and turbulence were measured

with the Meteorological Measurements System (MMS; Scott et al. 1990). The humidity conditions were measured by several instruments (Rollins et al. 2014). We used the water vapor mixing ratio measurements of the Harvard water vapor (HWV) instrument because it provided the most continuous dataset (Rollins et al. 2014). The HWV instrument is a combination of a Lyman-$\alpha$ photofragment fluorescence instrument and a tunable diode laser (TDL) direct absorption instrument. The sampled air is lead into two ducts, whereas the TDL measures in the first duct the water vapor absorption spectrum from which the water vapor concentration is calculated (Sargent et al. 2013). In the second duct, a Lyman-$\alpha$ lamp photodissociates the water vapor in the air and the fluorescent emissions from the OH ions are detected, from which the water vapor volume mixing ratio is calculated (Weinstock et al. 2009; Rollins et al. 2014). The used data sheet for these measurements, available from NASA (2012), gives an uncertainty of 7.5% due to calibration, 0.11 ppmv from instrument precision and up to 0.3 ppmv from potential instrument bias.

## 4. Case study—13 April 2011

On 13 April 2011, a synoptic cirrus cloud formed east of the Rocky Mountains, over Texas, driven by a southwesterly flow from the Pacific Ocean. The cirrus started to form in the afternoon UTC, grew during the evening, and reached its maximum intensity around midnight. The cirrus disappeared by the morning of the following day. As typical for this weather situation, no precipitation was observed.

### *a. MACPEX measurements results*

The aircraft took off at 1700 UTC and flew northwestward up to a height of about 14.6 km. At 1800 UTC, the aircraft reached the tail of the cirrus and descended into the cirrus top at about 10.5-km altitude. At 2000 UTC, the aircraft ascended again and returned to its starting point at Ellington Field, Houston (see Fig. 1). This day was chosen for our study because a robust dataset of IRP composition from PALMS measurements is available, and suggests the dominance of heterogeneous ice nucleation mainly driven by mineral particles. The composition of the IRPs for the measurements on 13 April 2011, shown in Fig. 2, is an unpublished subset of the published data in Cziczo et al. (2013). The evaluation and particle classification was performed as described in Cziczo et al. (2013) and briefly summarized in section 3.

For the day of interest, 43% of the detected IRPs were found to be mineral dust. About one-tenth of all IRPs were classified as biomass-burning particles indicated by organic- and BC-rich particles with potassium and a lack of crustal metals (Hudson et al. 2004). Particles with a high elemental carbon (EC) mass fraction were not present as IRPs.

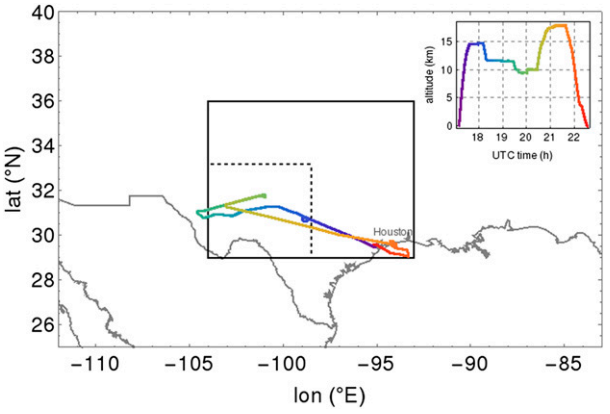


FIG. 1. Map of the flight path of the research aircraft on 13 Apr 2011. The colors indicate the time-dependent altitude of the aircraft shown in the inset in the upper-right corner. The black rectangle shows the model domain and the dashed box inside the domain where the modeling results were evaluated.

The internal mixtures of sulfate and organics, and sea salt particles (about 30% of all IRPs) may act as INP when present as glasses or anhydrous salts as described by Cziczo et al. (2013). However, homogeneous ice nucleation of supercooled droplets containing sulfate or sea salts is more likely and dominance of these as IRPs can be interpreted as homogeneously frozen particles.

From the SP2 measurements on this day, about 58% of all detected BC-containing particles were internally mixed. Of these, many almost bare BC particles and a few very thickly coated particles were found. This finding might indicate a mixing of biomass-burning-loaded air masses and air masses from other soot source regions, because for pure biomass-burning cases a higher fraction of mixed particles would be expected (Schwarz et al. 2008). In the cloud, about 51% of the detected BC-containing particles were still internally mixed, suggesting that nucleation processes did not preferentially remove internally mixed BC particles from the interstitial population.

### *b. Model setup*

Figure 1 shows the model domain (black rectangle) covering the area from 20° to 36°N and from −104° to −93°E. The observed cirrus cloud was situated approximately inside the black dashed box. The model is run with a horizontal grid spacing of 7 km and 40 vertical layers up to a height of 22.7 km. The simulation started

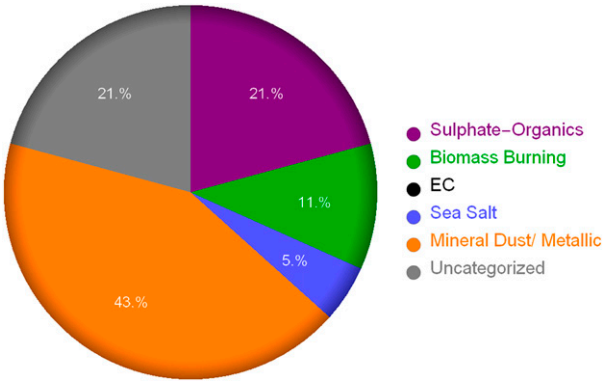


FIG. 2. Composition of IRP measured on 13 Apr 2011 with the PALMS instrument.

at 0000 UTC 12 April 2011 and ended at 0000 UTC 14 April 2011 with an output interval of 1 h.

The simulation was driven by meteorological data from the global model GME of the German Meteorological Service (data provided by Heike Vogel, KIT). The initial and boundary data for the gas-phase species concentrations in the ART module were provided by Model for Ozone and Related Chemical Tracers 4 (MOZART-4; Emmons et al. 2010; data obtained from https://www.acom.ucar.edu/wrf-chem/mozart.shtml) data. The dataset was preprocessed so that the MOZART-4 species match the gas-phase species of the ART module following Table 7 in Emmons et al. (2010). The anthropogenic emissions of ozone precursors, acidifying gases, particulate matter, and BC were given by the Emissions Database for Global Atmospheric Research Hemispheric Transport of Air Pollution, version 1 (EDGAR HTAPv1; Janssens-Maenhout et al. 2012; data obtained from http://edgar.jrc.ec.europa.eu/archived_datasets.php), dataset and was also preprocessed to match the aerosol/gas-phase species of the ART module. Thereby, the nonmethane volatile organic compounds (NMVOC) class was distributed to the different gas-phase species of ART and the given $NO_x$ emissions were first classified by traffic and nontraffic emissions according to their United Nations Framework Convention on Climate Change (UNFCCC) category and afterward apportioned to 90% (83%) NO and 10% (17%) $NO_2$ from traffic (nontraffic; Grice et al. 2009; Knote 2012). The BC class was attributed to the pure soot class in ART. Biogenic emissions were evaluated from the land-cover classifications given by the Global Land Cover (GLC; data obtained from Heike Vogel, KIT) dataset for the year 2000 and the Fraction of Green Vegetation Cover (FCOVER; data obtained from Konrad Deetz, KIT) dataset. For local dust emissions inside the model domain the Harmonized World Soil Database (HWSD; data obtained from Konrad Deetz, KIT) was used, while for dust potentially transported into the domain, dust concentrations were previously simulated for April 2011 using the Icosahedral Nonhydrostatic (ICON)-ART (Rieger et al. 2017) model. Additionally, local biomass-burning emissions were treated with a plume rise model in the ART module (Walter et al. 2016) using the Global Fire Assimilation System (GFAS), version 1, fire dataset (data obtained from http:/www.gmes-atmosphere.eu/about/project_structure/input_data/d_fire/). The dataset was also preprocessed to match the ART name conventions and the bcfire emissions were attributed to the pure soot class in ART. The formation and interaction of the internally mixed particle classes is treated within the ART module.

The enhanced number of biomass-burning particles found by PALMS and SP2 measurements is attributed in part to numerous wildfires inside and outside the domain preceding and throughout the simulation episodes. Drought conditions in spring 2011 (Nielsen-Gammon 2011) likely favored open burns. The datasets to initialize the model underestimated the measured soot concentration by several orders of magnitude. The SP2 instrument observed on 13 April 2011 a BC mass concentration above the boundary layer of $(2.7 \pm 0.81) \times 10^{-3}\,\mu g\,m^{-3}$ [data available from NASA (2012)] that lies in the typical range for the UTLS (Murphy et al. 2014). Therefore, the model internal minimum (pure) soot mass concentration was increased from $0.75 \times 10^{-9}$ to $2.0 \times 10^{-3}\,\mu g\,m^{-3}$.

The global ICON-ART simulations used to initialize the model dust concentration showed a significant dust transport event moving over the northern Pacific Ocean into the western part of the United States at this time (see Fig. 3 for accumulation mode dust mass concentration at 6 km with an initial median diameter of 1.5 $\mu$m; Rieger et al. 2017). Despite the initialization with this dataset, the model underestimated the dust concentration by several orders of magnitude. Therefore, we scaled the ICON-ART dust accumulation mode concentrations uniformly over the whole time, horizontal, and vertical range to match approximately the PALMS-observed clear-sky campaign averaged dust concentrations above the boundary layer (campaign average is $18.5 \times 10^4\,m^{-3}$). All simulations shown in the next section use the adjusted aerosol concentrations.

Table 2 lists the four variations of the heterogeneous ice nucleation parameterizations, which were applied in this study. First, the U17 scheme was applied with the standard parameter setup for soot and desert dust (U17 std). The soot ice nucleation active surface site (INAS) density parameterization of the U17 framework is only

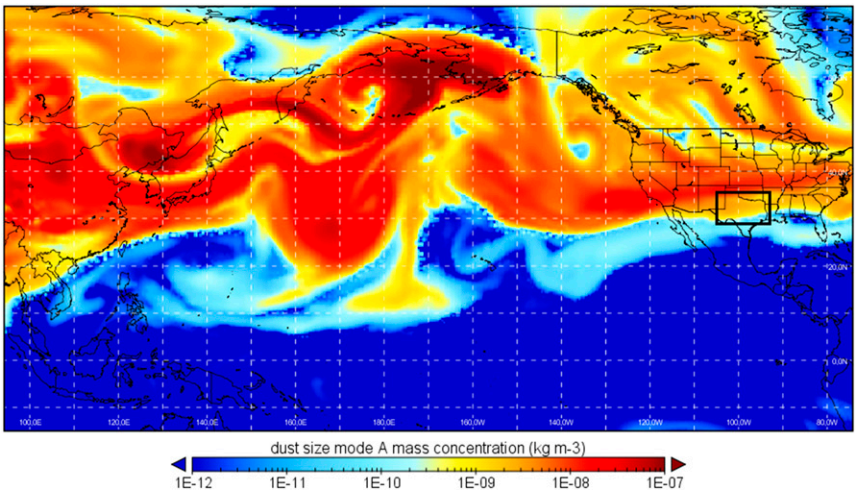


FIG. 3. Accumulation-mode dust mass concentration from global ICON-ART simulation at 1200 UTC 13 Apr 2011 at an altitude of 6 km. The black rectangle shows the model domain.

valid for laboratory-generated soot with a low organic compound (OC) content. Second, the parameterization for soot of the U17 scheme was scaled to predict aged soot/soot from biomass-burning plumes (U17 BB) because of the numerous wildfires in this season and region and hence, for a better representation of the measured IRP composition in the model. For that, we used AIDA cloud chamber experiments with soot with a higher OC content (diesel soot, mCAST_minOC, and CAST_maxOC; see Fig. A1 in the appendix; data taken from U17), which show a decreased ice nucleation ability (U17). From these experiments we derived a scaling factor of 0.01 for the INAS density parameterization [Eq. (A6)]. The P13 scheme was applied with the parameter setup for soot particles from biomass-burning plumes (P13 BB). Although the applied INP parameterization schemes are limited to a specific soot type, soot from both natural and anthropogenic sources are used to simulate the INP composition in this case study. Further, note that the biomass-burning particles measured by the PALMS instrument were identified by organic- and BC-rich particles in the mass spectra. Here we assume that these biomass-burning particles also include some soot and thus can be compared to the modeled soot INP. Third, to simulate aged dust, for example, from atmospheric transport, we used results from AIDA ice nucleation experiments with secondary organic aerosol (SOA) and sulfuric acid–coated Arizona test dust (ATD) and illite (Möhler et al. 2008; Cziczo et al. 2009) and estimated a scaling factor of 0.05 for the dust INAS density parameterization function (U17 aged dust).

Note that the model results presented in the following are evaluated for the subdomain in Fig. 1.

### c. *Comparison of modeled and measured ice nucleation*

First, comparing the aerosol profiles (Fig. 4) shows that in the range between 5- and 12-km height the modeled (U17 std simulation only) and measured dust number concentration agree within half an order of magnitude. Above 12-km height (above the levels used for comparison of the IRP) the modeled dust number concentration decreases rapidly to the prescribed minimum value (see Fig. 4). The agreement is satisfactory taking into account that we only scaled the dust accumulation mode with the PALMS profile. In the model simulation, the soot number concentration is about one order of magnitude (black lines in Fig. 4) higher than the SP2 BC-containing particle concentration. This could be explained by the fact that we scaled the model internal minimum pure soot mass concentration to match the SP2-measured BC-containing

TABLE 2. List of model simulations presented in this study. All model simulations use the same model setup, but different setups of the heterogeneous ice nucleation parameterizations.

| Simulation | Description |
|---|---|
| U17 std | U17 parameterization with default configuration |
| U17 BB | U17 parameterization with scaled INAS density for soot to predict ice nucleation biomass-burning particles and default configuration for dust |
| P13 BB | P13 parameterization with parameter $F_{OC} = 0$ and $\Xi = 1$ to simulate biomass-burning particles |
| U17 aged dust | U17 parameterization with scaled INAS density for dust to predict aged dust particles and default configuration for soot |

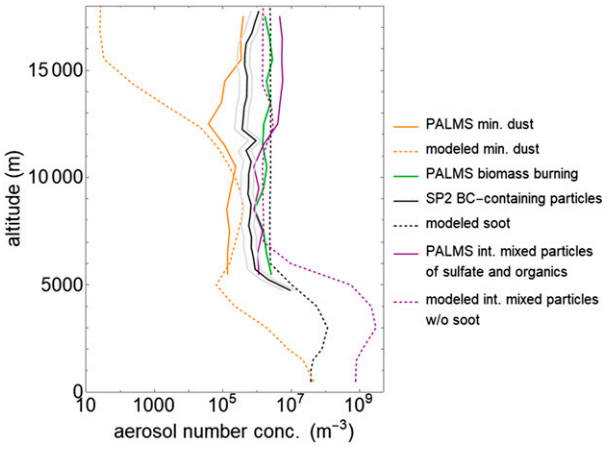


FIG. 4. Vertical profiles of the aerosol number concentrations. The solid lines show aerosol concentrations obtained from clear-sky PALMS (MACPEX campaign average) and SP2 aircraft measurements during the whole flight on 13 Apr 2011 [data available from NASA (2012)] excluding takeoff and landing. The gray lines indicate the SP2 measurement uncertainty of 40%. The dashed lines show modeled aerosol concentrations (U17 std simulation run) averaged over the model subdomain and averaged in time between 1800 and 2100 UTC.

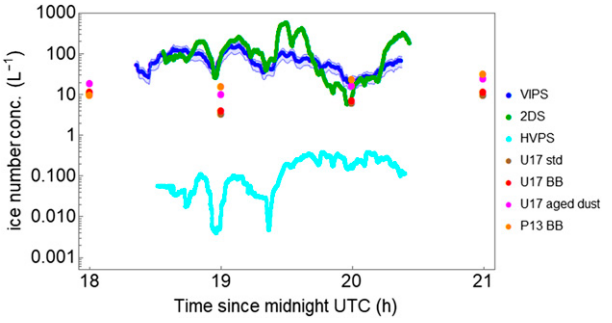


FIG. 5. Ice number concentrations measured by VIPS, 2D-S and HVPS on 13 Apr 2011 above the boundary layer and time averaged for 300 s [data available from NASA (2012)]. The reddish points show the ice particle number concentrations for the four simulation cases averaged between 1800 and 2100 UTC and between 8 and 12 km.

particle mass concentration. However, the model distributes this mass in part to particle sizes smaller than the SP2 detection limit, which will lead to an overestimation of the model soot number concentration associated with the given mass. The biomass-burning particle class concentration measured by PALMS (MACPEX campaign average), which includes biomass-burning-sourced particles without BC content, shows higher concentrations than the SP2. However, the observed mixing state of the BC-containing particles from the SP2 measurements indicate the strong influence of soot from biomass-burning plumes and hence supports the high concentration observed by the PALMS instrument. The secondary internally mixed particle concentrations (purple lines) agree well between 5 and 11 km. Above 11 km, the modeled concentration is higher than the PALMS MACPEX campaign average. Please note that the modeled aerosol profiles as shown in Fig. 4 do not change for the other simulation runs because aerosol depletion due to activation is not implemented in the COSMO-ART model.

The VIPS and 2D-S ice particle concentration agree in the overlapping time range within a factor of about ±5 (Fig. 5). However, the 2D-S shows mostly somewhat higher concentrations than the VIPS. This might be explained by an overestimation of the particle concentration in the very first size bin of the 2D-S instrument due to the uncertainty in the depth of field (Jensen et al. 2013).

The ice number concentration measured by the HVPS [data available from NASA (2012) and time averaged to 300 s] is about three orders of magnitude lower than the concentrations from VIPS and 2D-S. This is because the observed cirrus cloud was not forming precipitating ice particles like snow and the HVPS instrument measured only the very large ice particles in its smallest-size bins. Therefore, we exclude the HVPS measurements for our comparison. In comparison, the modeled ice particle concentrations shown in reddish in Fig. 5 are lower than the measured concentration, but agree within a factor of about 10 to the 2D-S measured ice particle concentration in the overlapping time range. From 1900 UTC on, the U17 aged dust and P13 BB simulation cases show higher concentrations than the U17 std and BB cases indicating a somewhat different INP composition. However, ice number concentrations of less than 100 particles per liter found in the model as well as in the measurements on 13 April 2011 indicate the dominance of heterogeneous ice nucleation (Cziczo and Froyd 2014).

The contribution of the different ice nucleation mechanisms is partly determined by the updraft velocity. The vertical velocity distributions measured during MACPEX flights (shown by Jensen et al. 2013) were non-Gaussian, with a tail to high vertical velocities, which the parameterization of subgrid vertical velocities cannot represent. In Fig. 6, we compare the ice saturation ratio, which is influenced by the vertical velocity, but also by vapor deposition to existing particles. Since the ice saturation ratio increases within the updraft, $S_i$ exceeds at a certain point 1.0 and ice nucleation can take place and depletes water vapor. Hence, the increase in $S_i$ flattens and reaches a maximum. Since ice particles from heterogeneous ice nucleation form earlier (e.g., at lower $S_i$) and, therefore, water vapor is

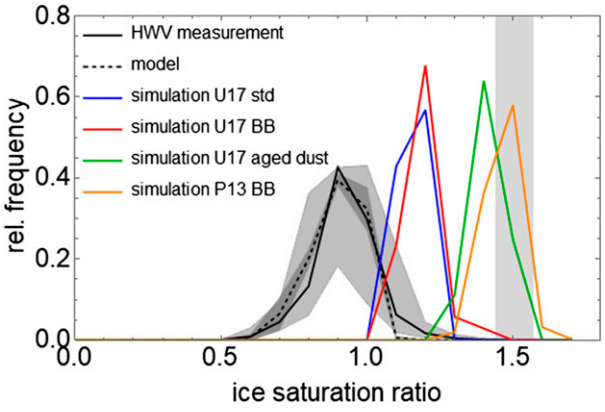


FIG. 6. Relative frequency of measured and modeled ice saturation ratios. The black line is calculated from the HWV water vapor mixing ratio measurements between 1800 and 2100 UTC 13 Apr 2013 [data available from NASA (2012)] for times when the 2D-S instrument indicated more than 10 particles per liter. The uncertainty range of the HWV data is given by the light gray shaded area. The black dashed line is the mean grid-scale $S_i$ for all four simulations and the dark gray shaded area is the standard error of the mean. The colored lines show the relative frequency of the maximum ice saturation ratio reached for ice nucleation in the model. The light gray shaded bar indicates the threshold ice saturation ratio for homogeneous freezing at temperatures of 224.543 ± 9.212 K [subdomain model average for U17 std simulation; $S_{i,\mathrm{hom}}$ calculated from Ren and MacKenzie (2005)].

consumed over a longer time, the maximum in $S_i$ is lowered. If the INP concentration is large enough, $S_i$ does not reach the homogeneous freezing threshold $S_i$ and homogeneous freezing is suppressed. The HWV water vapor mixing ratio was converted to an ice saturation ratio $S_i$ using the MMS temperature and pressure measurements [both datasets available from NASA (2012)]. The measured $S_i$ reached very rarely the threshold for homogeneous ice nucleation (gray shaded area in Fig. 6) supporting the indication from the ice particle measurements that heterogeneous ice nucleation might had dominated the primary ice formation on this day. In comparison, the model grid-mean $S_i$ values (mean for the four simulations) are frequently lower than the measured values. As mentioned in section 2a, ice nucleation in the model takes place at a parameterized subgrid-scale ice saturation ratio $S_{i,\mathrm{max}}$ (Barahona and Nenes 2009a,b). This maximum $S_i$ is shown by the colored lines in Fig. 6 for the four simulation runs and indicates the dominating ice nucleation mechanism. For the simulations U17 std and U17 BB, $S_i$ does not reach the homogeneous freezing threshold, indicating that homogeneous ice nucleation is almost suppressed. In the simulations U17 aged dust and P13 BB, $S_i$ exceeds the homogeneous freezing threshold, where the threshold is reached more often in case of the P13 BB simulation.

### *d. Comparison of modeled INP and measured IRP*

The dominance of mineral dust in the IRP composition measured by the PALMS instrument (see Fig. 2) suggests that heterogeneous ice nucleation dominated cirrus formation on this day. The other IRP types can initiate ice nucleation either homogeneously or heterogeneously. Biomass-burning particles are composed of up to 10% BC soot (Reid et al. 2005), which may act as a heterogeneous INP. However, note the lack of bare EC particles in the IRP composition (for particle diameters larger than 200 nm). Particles composed of mixtures of sulfates and organics or sea salt can act as INP when present as glasses (e.g., Abbatt et al. 2006; Wagner et al. 2012) or anhydrous salts (Wagner et al. 2018). On 13 April 2011, in-cloud temperatures from 215 to 220 K and ice saturation ratios of up to 1.4 [temperature data from the MMS and relative humidity ($\mathrm{RH}_i$) data from the HWV are available from NASA (2012)] could have enabled heterogeneous ice nucleation of these particles.

The comparisons in the previous section indicated that the simulations with the U17 parameterization scheme predict the dominance of heterogeneous ice nucleation on this day as found by the measurements. Indeed, the fraction of homogeneously frozen droplets in the case U17 std and U17 BB is only about 0.2% (see Table 3), whereas observations suggest that approximately 21% of the ice is formed by homogeneous freezing. Heterogeneous ice nucleation is dominated by dust particles as found by PALMS. However, the strong suppression of homogeneous ice nucleation as well as the large fraction of soot INP (≈44%) in case of the U17 std simulation suggests that the parameterization developed for laboratory-generated low-OC soot is not able to predict the measured IRP composition. Changing the model to predict soot INP from biomass-burning plumes alters the results, which is also different from the P13 BB simulation. The INP composition from the P13 BB simulation shows only a minor contribution of heterogeneous ice nucleation (about 6%). Furthermore, soot INPs dominate the heterogeneous ice nucleation instead of dust INPs. Hence, the INP composition in simulation P13 BB is very different from the measured IRP composition. In case of the U17 BB simulation, the contribution of soot INP is comparable to the P13 BB simulation. In the P13 BB simulation homogeneous freezing of solution droplets dominates. However, the dominance of dust INP in the case of the U17 BB simulation is

TABLE 3. Fraction (%) of homogeneously frozen droplets and heterogeneous ice nucleation on soot and dust particles predicted with the COSMO-ART model applying the P13 and the U17 parameterization schemes as summarized in Table 2. The values are averages for the model subdomain between 8 and 12 km.

| | U17 std | U17 BB | U17 aged dust | P13 BB |
|---|---|---|---|---|
| Hom freezing | 0.16 | 0.20 | 48.38 | 93.79 |
| Dust | 56.48 | 96.45 | 21.46 | 1.12 |
| Soot | 43.36 | 3.35 | 30.16 | 5.09 |

qualitatively in better agreement with the PALMS IRP composition. Taking into account that 1) the model soot concentration might be overestimated in comparison to the SP2-measured BC-containing particle concentration and 2) the scaling of the U17 parameterization function for dust particles was only a rough estimation, the best agreement between modeled INP and measured IRP is achieved with the U17 aged dust simulation. Note that sea salt particles are assumed to solely contribute to homogeneous ice nucleation in the COSMO-ART model.

## 5. Conclusions

In this study, we compared modeled INP composition with measured IRP composition. We used the COSMO-ART model with two different parameterizations of heterogeneous ice nucleation for mineral dust and soot aerosol particles (P13; U17). The IRP composition was measured by the PALMS instrument during the MACPEX campaign in spring 2011. We selected April 13 for this case study because, during this day, the measurements indicated the dominance of heterogeneous ice nucleation. The IRP composition was dominated by mineral dust and biomass-burning particles, because the probed cirrus cloud was strongly influenced by a drought in the south-central United States and biomass-burning exhaust from local and more distant wildfires.

All model simulations showed good agreement of the ice particle concentration with the measurements of VIPS and 2D-S on this day. However, the simulation with the P13 scheme reached ice saturation ratios indicating the dominance of homogeneous ice nucleation, whereas the simulations with the U17 scheme indicated the dominance of heterogeneous ice nucleation. These findings are supported by the comparison of the IRP–INP composition. Although the parameterization scheme of P13 provides parameterizations for heterogeneous ice nucleation on dust as well as soot originating from biomass burning, the modeling results using this parameterization show a majority of homogeneously frozen solution droplets in disagreement with the PALMS IRP measurements. This potential underestimation of heterogeneous INPs compared to other parameterization schemes was also found by other modeling studies (e.g., Barahona et al. 2010; Sullivan et al. 2016). A possible explanation for this underestimation was given by U17 who compared their parameterization scheme with this of P13. They argued that the P13 scheme would only give significant INP concentrations near the homogeneous freezing level where the homogeneous freezing of solution droplets is more likely. Although the U17 scheme is able to reproduce the overall dominating primary ice formation mechanism, the U17 std and U17 BB simulations underestimate homogeneous freezing compared to the PALMS measurement. The U17 aged dust simulation agrees slightly better, but the parameter adjustment is based on only a few AIDA measurements with nonnatural dust. It may be that the U17 simulations overestimate heterogeneous INP concentration because depletion of aerosol due to INP activation is not treated in the model.

Furthermore, the simulations with the U17 scheme indicate the strong influence of dust aerosol to cirrus ice formation, because the soot aerosol seems to be unable to suppress homogeneous ice nucleation as effectively as dust aerosol does. Nevertheless, soot (from anthropogenic and natural sources) has to be taken into account when simulating heterogeneous ice nucleation in cirrus clouds. This is difficult, because of the diverse ice nucleation activities of different soot types (perhaps depending on the OC fraction $F_{OC}$; U17). P13 suggests that the fraction of insoluble organic matter (internally) mixed with the BC particles scales with the ice nucleation ability of soot particles. This approach has possibly two weak points: 1) $F_{OC}$ is a highly uncertain measure mainly because of the uncertainties of the OC-content determination (Reid et al. 2005) and 2) soluble coatings (e.g., sulfuric acid or SOA) reduce the ice nucleation ability of soot (Möhler et al. 2005; Crawford et al. 2011) but are not taken into account by adjusting the soot-specific ice nucleation efficiency. Thus, the scaling with $F_{OC}$ appears insufficient for a correct description of soot originating from biomass burning, at least in this case. Hence, more laboratory experiments with soot with a higher OC content (e.g., biomass-burning particles or coated soot) and aged natural dust aerosol are needed to validate these adjustments.

Another caveat is that the quantitative comparison to the PALMS IRP measurements has some limitations because these measurements are only based on a small number of classified IRP sampled across the flight path

of the aircraft (Table S1 in Cziczo et al. 2013; 31% for the heterogeneous cirrus cases during the MACPEX campaign). Due to impaction issues and limitation in the ice crystal residence time, only smaller ice particles can be probed (Cziczo and Froyd 2014). It might be that larger ice particles contain different IRP. Furthermore, breakup of ice particle on the inlet might enhance the number of small-mode IRP, but was found to be not dominant (Field et al. 2003). In contrast, the model results are evaluated for the whole model domain and have a low spatial resolution. Furthermore in the COSMO-ART model, aerosol particles that can potentially act as INP, for example, sea salt at cirrus temperatures (Wagner et al. 2018), are not treated due to missing parameterizations for the heterogeneous ice nucleation ability. Often, a lack of comprehensive measurements, for example, aerosol size distribution over the full size range, hamper 1) the correct initialization of the model and 2) the interpretation of the model results.

This study shows that we are not yet able to accurately reproduce measured IRP compositions but we think the application of the U17 scheme points into the right direction. Further, the study shows that we are making progress in 1) bringing field, laboratory, and modeling work together and 2) gaining a better representation of aerosol–cloud interaction needed for a better understanding of, for example, aerosol climate effect (e.g., Storelvmo 2017) by improving parameterizations of heterogeneous ice nucleation.

*Acknowledgments.* The authors thank Dr. Heike Vogel and Konrad Deetz for providing the GLC, FCOVER, HWSD, and GME datasets. Further, the authors thank Dr. Dominik Brunner for his assistance to preprocess the EDGAR HTAP v1 dataset.

We thank the NASA WB-57F flight and ground crews and the MACPEX participants. We also thank the NASA Earth Science Division Atmospheric Composition program (Award NNH11AQ58UI and Grant NNX13AO15G), the NOAA Atmospheric Chemistry, Carbon Cycle and Climate program (3RR1GFKP00), the NASA Radiation Science program (Award NNH14AX25I), the NASA Upper Atmospheric Research program (Grant NNH09ZDA001N-MACPEX) and the NASA MACPEX research project funding (NNX11AC07G).

This research was partly funded by the Helmholtz Association through the Helmholtz Climate Initiative REKLIM and the President's Initiative and Networking Fund, and partly funded by the Deutsche Forschungsgemeinschaft (DFG) through the research unit INUIT (FOR 1525, Projects HO4612/1-1, HO4612/1-2, MO 668/4-1, and MO 668/4-2).

## APPENDIX

### Parameterization Schemes for Heterogeneous Ice Nucleation

#### *a. P13 parameterization*

P13 is based on the work of Phillips et al. (2008), but updates some of the parameters. In the scheme of Phillips et al. (2008) the number of INPs of aerosol species $X$ is calculated via

$$n_{\mathrm{INP},X} = \int_{\log(0.1\mu\mathrm{m})}^{\infty} \{1 - \exp[-\mu_X(D_X, T, S_i)]\} \times \frac{dn_X}{d\log D_X} d\log D_X, \quad \text{(A1)}$$

for temperatures ranging between 273 and 193 K for dust and 198 K for soot. In the above equation, $D_X$ is the aerosol volume-equivalent diameter, $n_X$ is the aerosol number concentration, and $\mu_X$ is the number of aerosol particles of species $X$ activated to ice;

$$\mu_X = H_X(S_i, T)\xi_X(T)\frac{\alpha_X n_{\mathrm{IN},1,*}}{\Omega_{X,1,*}}\frac{d\Omega_X}{dn_X}. \quad \text{(A2)}$$

The variable $n_{\mathrm{IN},1,*}$ represents the reference activity spectrum, partly obtained from CFDC (Rogers et al. 2001) measurements in various field campaigns (e.g., DeMott et al. 2003). However, the measurements were only conducted at temperatures below 233 K. For temperatures above 248 K, Phillips et al. (2008) rescaled the parameterization of Meyers et al. (1992), and for temperatures between 248 and 233 K, Phillips et al. (2008) interpolated between this and the parameterization obtained from the CFDC measurements. The variable $\Omega_{X,1,*}$ is the contribution of the total background aerosol surface area concentration of species $X$ for particles with diameters between 0.1 and 1 $\mu$m. This area concentration is $2.0 \times 10^{-6}\,\mathrm{m^2\,kg^{-1}}$ for mineral dust, and $1.0 \times 10^{-7}\,\mathrm{m^2\,kg^{-1}}$ for soot (P13). Assuming spherical particles, the last term in Eq. (A2) is approximated by $d\Omega_X/dn_X \approx \pi D_X^2$.

In Eq. (A2) $\alpha_X$ is the prescribed fraction of aerosol $X$ contributing to ice nucleation. For mineral dust, this parameter is a constant of 2/3. For soot, this fraction is controlled by the hydrophilicity $\Xi$: $\alpha_{\mathrm{BC}} = (1/3 - 0.03)\,\Xi(P_S, F_{\mathrm{OC}})$ (P13). The hydrophilicity is determined by the surface polarity $P_S$, meaning the number of water monolayers

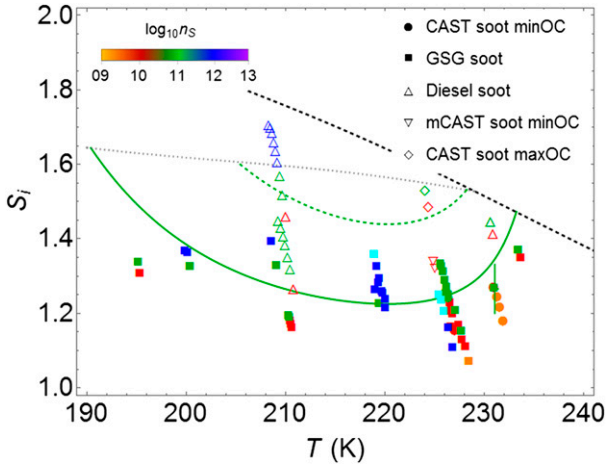


FIG. A1. INAS densities as a function of temperature and ice saturation ratio for deposition nucleation on soot (redrawn from U17). The black dashed lines shows the ice saturation ratio at water saturation and the dotted line the homogeneous freezing threshold ($\Delta a_w = 0.34$; Koop et al. 2000). The different symbols indicate different samples and the different colors the order of magnitude of the INAS density. The filled symbols indicate the soot samples on which the default parameterization is based and the open symbols indicate the soot samples with a higher OC content contributing to the scaling factor for the INAS density. The solid green line shows the contour line for $n_S = 10^{11}$ m$^{-2}$ of the parameterization as given by U17 and the dashed line the scaled parameterization.

absorbed by the particles surface at 50% relative humidity (P13), and the fractional coverage of the particle surface by insoluble organics $F_{OC}$. Hence, the P13 scheme provides an INP parameterization for soot from different sources. In the case of particles originating from biomass-burning plumes, the hydrophilicity $\Xi$ is about 1, where $F_{OC} \simeq 0$ and $P_S > 2$ (P13). Thereby, P13 assumes that these particles were coated with inorganics and volatile organics during the early stage of particle formation and became internally mixed with insoluble organics during transport. Particles from fresh urban fossil fuel pollution are assumed to be more hydrophobic ($\Xi \simeq 0$) than the particles from biomass-burning plumes.

The term $\xi$ suppresses droplet freezing above 271 K and $H_X \in [0, 1]$ takes into account the scarcity of heterogeneous ice nucleation below water saturation, while $H_X \equiv 1$ at water saturation:

$$H_X(S_i, T) = \min\{f_{C,X} + (1 - f_{C,X}) \times \delta_0^1[S_w(S_i, T), 0.97, 1], 1\}, \quad \text{(A3)}$$

where $\delta$ is a cubic interpolation function and $f_{C,X}$ represents the fraction of deposition ice nucleation to total ice nucleation. This contribution depends on the aerosol-specific ice nucleation threshold temperature and the ice saturation ratio. For soot particles, the threshold ice saturation ratio depends again on the fractional coverage of insoluble organics $F_{OC}$. This means that for low $F_{OC}$, as in the case of biomass-burning particles, the threshold ice saturation ratio is lower than for BC more thickly coated with organics.

### b. *U17 parameterization*

The framework of U17 is solely based on experiments at the AIDA (e.g., Möhler et al. 2003) cloud chamber conducted on a wide range of atmospherically relevant temperatures and relative humidities, especially at cirrus temperatures (Fig. A1). Experiments on heterogeneous ice nucleation of different natural desert dusts and laboratory-generated soot with different OC content were reevaluated and used to develop a new INAS (e.g., Hoose and Möhler 2012; Murray et al. 2012; Vali et al. 2015) density-based heterogeneous ice nucleation scheme. The number of INP of aerosol species $X$ is calculated via

$$n_{\mathrm{INP},X} = \sum_k n_{X,k}\left\{1 - \exp[-n_{S,X}(T, S_i)\, S_{X,k}]\right\}, \quad \text{(A4)}$$

where $n_{X,k}$ is the number concentration of aerosol species $X$ and $S_{X,k}$ the corresponding surface area in size mode $k$, both given by the aerosol spectrum in the model. From the laboratory observations, the INAS density is calculated by

$$n_S(T, S_i) = \frac{n_{\mathrm{ice}}(T, S_i)}{s_{\mathrm{ae}}}, \quad \text{(A5)}$$

based on the singular approach (Connolly et al. 2009; Vali et al. 2015), where $n_{\mathrm{ice}}$ is the ice particle concentration and $s_{\mathrm{ae}}$ the available aerosol surface area concentration obtained from size distribution measurements (U17). From the reevaluation of the experiments U17 obtained

TABLE A1. Fit parameters of Eq. (A6) for desert dust and soot with an organic carbon content of less than or equal 20% wt (U17). The parameterization is only valid for ice saturation ratios ranging from 1.0 to the homogeneous freezing threshold and water saturation, respectively.

| Aerosol | $\alpha$ | $\beta$ | $\gamma$ | $\kappa$ | $\lambda$ | Valid $T$ range (K) |
|---|---|---|---|---|---|---|
| Desert dust | 285.692 | 0.017 | 256.692 | 0.080 | 200.745 | [206, 240] |
| Soot | 46.021 | 0.011 | 248.560 | 0.148 | 237.570 | [195, 235] |

an INAS density parameterization function for the relevant temperature range:

$$n_{S,X}(T,S_i) = \exp\{\alpha(S_i - 1)^{1/4}\cos[\beta\ (T-\gamma)]^2 \times \operatorname{arccot}[\kappa\ (T-\lambda)]/\pi\}\ \mathrm{m}^{-2}, \quad \text{(A6)}$$

$$\operatorname{arccot}(x) := \frac{\pi}{2} - \arctan(x).$$

This parameterization function is valid for $1.0 \le S_i \le S_{i,\mathrm{hom}}$, where $S_{i,\mathrm{hom}}$ is the homogeneous freezing threshold (e.g., Koop et al. 2000; Ren and MacKenzie 2005). The parameters and valid temperature ranges for Eq. (A6) are listed in Table A1. U17 found a dependency of the ice nucleation ability of soot on its organic carbon content. That means that soot with a higher organic carbon content requires a higher ice saturation ratio to reach the same INAS density as soot with a low organic carbon content at the same temperature. The parameterization is only valid for soot with a low organic carbon content (less than 20% wt; see Table 7 in U17).

## REFERENCES


Abbatt, J. P. D., S. Benz, D. J. Cziczo, Z. Kanji, U. Lohmann, and O. Möhler, 2006: Solid ammonium sulfate aerosols as ice nuclei: A pathway for cirrus cloud formation. *Science*, **313**, 1770–1773, https://doi.org/10.1126/science.1129726.

Baldauf, M., A. Seifert, J. Förstner, D. Majewski, M. Raschendorfer, and T. Reinhardt, 2011: Operational convective-scale numerical weather prediction with the COSMO model: Description and sensitivities. *Mon. Wea. Rev.*, **139**, 3887–3905, https://doi.org/10.1175/MWR-D-10-05013.1.

Bangert, M., and Coauthors, 2012: Saharan dust event impact on cloud formation and radiation over western Europe. *Atmos. Chem. Phys.*, **12**, 4045–4063, https://doi.org/10.5194/acp-12-4045-2012.

Barahona, D., and A. Nenes, 2008: Parameterization of cirrus cloud formation in large-scale models: Homogeneous nucleation. *J. Geophys. Res.*, **113**, D11211, https://doi.org/10.1029/2007JD009355.

——, and ——, 2009a: Parameterizing the competition between homogeneous and heterogeneous freezing in cirrus cloud formation—Monodisperse ice nuclei. *Atmos. Chem. Phys.*, **9**, 369–381, https://doi.org/10.5194/acp-9-369-2009.

——, and ——, 2009b: Parameterizing the competition between homogeneous and heterogeneous freezing in ice cloud formation—Polydisperse ice nuclei. *Atmos. Chem. Phys.*, **9**, 5933–5948, https://doi.org/10.5194/acp-9-5933-2009.

——, J. Rodriguez, and A. Nenes, 2010: Sensitivity of the global distribution of cirrus ice crystal concentration to heterogeneous freezing. *J. Geophys. Res.*, **115**, D23213, https://doi.org/10.1029/2010JD014273.

——, A. Molod, and H. Kalesse, 2017: Direct estimation of the global distribution of vertical velocity within cirrus clouds. *Sci. Rep.*, **7**, 6840, https://doi.org/10.1038/s41598-017-07038-6.

Boucher, O., and Coauthors, 2013: Clouds and aerosols. *Climate Change 2013: The Physical Science Basis*, T. F. Stocker et al., Eds., Cambridge University Press, 571–658, https://doi.org/10.1017/CBO9781107415324.016.

Connolly, P., O. Möhler, P. Field, H. Saathoff, R. Burgess, T. Choularton, and M. Gallagher, 2009: Studies of heterogeneous freezing by three different desert dust samples. *Atmos. Chem. Phys.*, **9**, 2805–2824, https://doi.org/10.5194/acp-9-2805-2009.

Crawford, I., and Coauthors, 2011: Studies of propane flame soot acting as heterogeneous ice nuclei in conjunction with single particle soot photometer measurements. *Atmos. Chem. Phys.*, **11**, 9549–9561, https://doi.org/10.5194/acp-11-9549-2011.

Cziczo, D., and K. Froyd, 2014: Sampling the composition of cirrus ice residuals. *Atmos. Res.*, **142**, 15–31, https://doi.org/10.1016/j.atmosres.2013.06.012.

——, ——, S. Gallavardin, O. Möhler, S. Benz, H. Saathoff, and D. Murphy, 2009: Deactivation of ice nuclei due to atmospherically relevant surface coatings. *Environ. Res. Lett.*, **4**, 044013, https://doi.org/10.1088/1748-9326/4/4/044013.

——, and Coauthors, 2013: Clarifying the dominant sources and mechanisms of cirrus cloud formation. *Science*, **340**, 1320–1324, https://doi.org/10.1126/science.1234145.

DeMott, P., D. Cziczo, A. Prenni, D. Murphy, S. Kreidenweis, D. Thomson, R. Borys, and D. Rogers, 2003: Measurements of the concentration and composition of nuclei for cirrus formation. *Proc. Natl. Acad. Sci. USA*, **100**, 14 655–14 660, https://doi.org/10.1073/pnas.2532677100.

Doms, G., and M. Baldauf, 2015: A description of the nonhydrostatic regional COSMO-model—Part I: Dynamics and Numerics. Deutscher Wetterdienst Rep., 167 pp.

——, and Coauthors, 2011: A description of the nonhydrostatic regional COSMO-model—Part II: Physical parameterization. Deutscher Wetterdienst Rep., 161 pp.

Emmons, L., and Coauthors, 2010: Description and evaluation of the Model For Ozone And Related Chemical Tracers, version 4 (MOZART-4). *Geosci. Model Dev.*, **3**, 43–67, https://doi.org/10.5194/gmd-3-43-2010.

Field, P., R. Wood, P. Brown, P. Kaye, E. Hirst, R. Greenaway, and J. Smith, 2003: Ice particle interarrival times measured with a fast FSSP. *J. Atmos. Oceanic Technol.*, **20**, 249–261, https://doi.org/10.1175/1520-0426(2003)020<0249:IPITMW>2.0.CO;2.

Froyd, K., D. Murphy, T. Sanford, D. Thomson, J. Wilson, L. Pfister, and L. Lait, 2009: Aerosol composition of the tropical upper troposphere. *Atmos. Chem. Phys.*, **9**, 4363–4385, https://doi.org/10.5194/acp-9-4363-2009.

Gasparini, B., and U. Lohmann, 2016: Why cirrus cloud seeding cannot substantially cool the planet. *J. Geophys. Res. Atmos.*, **121**, 4877–4893, https://doi.org/10.1002/2015JD024666.

Gettelman, A., and Coauthors, 2010: Global simulation of ice nucleation and ice supersaturation with an improved cloud scheme in the Community Atmosphere Model. *J. Geophys. Res.*, **115**, D18216, https://doi.org/10.1029/2009JD013797.

Grice, S., J. Stedman, A. Kent, M. Hobson, J. Norris, J. Abbott, and S. Cooke, 2009: Recent trends and projections of primary $NO_2$ emissions in Europe. *Atmos. Environ.*, **43**, 2154–2167, https://doi.org/10.1016/j.atmosenv.2009.01.019.

Heymsfield, A., and L. Miloshevich, 1993: Homogeneous ice nucleation and supercooled liquid water in orographic wave clouds. *J. Atmos. Sci.*, **50**, 2335–2353, https://doi.org/10.1175/1520-0469(1993)050<2335:HINASL>2.0.CO;2.

——, and ——, 1995: Relative humidity and temperature influences on the cirrus formation and evolution: Observations from wave clouds and FIRE II. *J. Atmos. Sci.*, **52**, 4302–4326, https://doi.org/10.1175/1520-0469(1995)052<4302:RHATIO>2.0.CO;2.

——, and Coauthors, 2017: Cirrus clouds. *Ice Formation and Evolution in Clouds and Precipitation: Measurement and Modeling*

*Challenges. Meteor. Monogr.*, No. 58, Amer. Meteor. Soc., https://doi.org/10.1175/AMSMONOGRAPHS-D-16-0010.1.

Hoose, C., and O. Möhler, 2012: Heterogeneous ice nucleation on atmospheric aerosols: A review of results from laboratory experiments. *Atmos. Chem. Phys.*, **12**, 9817–9854, https://doi.org/10.5194/acp-12-9817-2012.

Hudson, P., and Coauthors, 2004: Biomass-burning particle measurements: Characteristic composition and chemical processing. *J. Geophys. Res.*, **109**, D23S27, https://doi.org/10.1029/2003JD004398.

Janssens-Maenhout, G., and Coauthors, 2012: EDGAR-HTAP: A harmonized gridded air pollution emission dataset based on national inventories. European Commission Joint Research Centre Tech. Rep., 43 pp.

Jensen, E., R. Lawson, J. Bergman, L. Pfister, T. Bui, and C. Schmitt, 2013: Physical processes controlling ice concentrations in synoptically forced midlatitude cirrus. *J. Geophys. Res. Atmos.*, **118**, 5348–5360, https://doi.org/10.1002/jgrd.50421.

——, and Coauthors, 2016: On the susceptibility of cold tropical cirrus to ice nuclei abundance. *J. Atmos. Sci.*, **73**, 2445–2464, https://doi.org/10.1175/JAS-D-15-0274.1.

Kamphus, M., and Coauthors, 2010: Chemical composition of ambient aerosol, ice residues and cloud droplet residues in mixed-phase clouds: Single particle analysis during the Cloud and Aerosol Characterization Experiment (CLACE 6). *Atmos. Chem. Phys.*, **10**, 8077–8095, https://doi.org/10.5194/acp-10-8077-2010.

Kärcher, B., and P. Spichtinger, 2009: Cloud-controlling factors of cirrus. *Clouds in the Perturbed Climate System: Their Relationship to Energy Balance, Atmospheric Dynamics, and Precipitation*, J. Heintzenberg and R. Charlson, Eds., MIT Press, 235–268.

Knote, C., 2012: Regional scale impact of changing anthropogenic emissions on aerosol. Ph.D. thesis, ETH Zurich, 131 pp.

Komurcu, M., and Coauthors, 2014: Intercomparison of the cloud water phase among global climate models. *J. Geophys. Res. Atmos.*, **119**, 3372–3400, https://doi.org/10.1002/2013JD021119.

Koop, T., B. Luo, A. Tsias, and T. Peter, 2000: Water activity as the determinant for homogeneous ice nucleation in aqueous solutions. *Nature*, **406**, 611–614, https://doi.org/10.1038/35020537.

Krämer, M., and Coauthors, 2016: A microphysics guide to cirrus clouds—Part 1: Cirrus types. *Atmos. Chem. Phys.*, **16**, 3463–3483, https://doi.org/10.5194/acp-16-3463-2016.

Lawson, R., 2011: Effect of the ice particles shattering on the 2D-S probe. *Atmos. Meas. Tech.*, **4**, 1361–1381, https://doi.org/10.5194/amt-4-1361-2011.

——, D. O'Connor, P. Zmarzly, K. Weaver, B. Baker, Q. Mo, and H. Jonsson, 2006: The 2D-S probe: Design and preliminary tests of a new airborne, high-speed, high-resolution particle imaging probe. *J. Atmos. Oceanic Technol.*, **23**, 1462–1477, https://doi.org/10.1175/JTECH1927.1.

——, B. Pilson, B. Baker, Q. Mo, E. Jensen, L. Pfister, and P. Bui, 2008: Aircraft measurements of microphysical properties of subvisible cirrus in the tropical tropopause layer. *Atmos. Chem. Phys.*, **8**, 1609–1620, https://doi.org/10.5194/acp-8-1609-2008.

Li, J.-L., and Coauthors, 2012: An observationally based evaluation of cloud ice water in CIMP3 and CIMP5 GCMs and contemporary reanalyses using contemporary satellite data. *J. Geophys. Res.*, **117**, D16105, https://doi.org/10.1029/2012JD017640.

Luebke, A., L. Avallone, C. Schiller, J. Meyer, C. Rolf, and M. Krämer, 2013: Ice water content of Arctic, midlatitude, and tropical cirrus—Part 2: Extension of the database and new statistical analysis. *Atmos. Chem. Phys.*, **13**, 6447–6459, https://doi.org/10.5194/acp-13-6447-2013.

Lundgren, K., B. Vogel, H. Vogel, and C. Kottmeier, 2013: Direct radiative effects of sea salt for the Mediterranean region under conditions of low to moderate wind speeds. *J. Geophys. Res. Atmos.*, **118**, 1906–1923, https://doi.org/10.1029/2012JD018629.

Lynch, D., K. Sassen, D. Starr, and G. Stephens, 2002: *Cirrus*. Oxford University Press, 480 pp.

McFarquhar, G., and A. Heymsfield, 1996: Microphysical characteristics of three anvils sampled during the Central Equatorial Pacific Experiment. *J. Atmos. Sci.*, **53**, 2401–2423, https://doi.org/10.1175/1520-0469(1996)053<2401:MCOTAS>2.0.CO;2.

Mellor, G., and T. Yamada, 1974: A hierarchy of turbulence closure models for planetary boundary layers. *J. Atmos. Sci.*, **31**, 1791–1806, https://doi.org/10.1175/1520-0469(1974)031<1791:AHOTCM>2.0.CO;2.

Meyers, M., P. DeMott, and W. Cotton, 1992: New primary ice-nucleation parameterizations in an explicit cloud model. *J. Appl. Meteor.*, **31**, 708–721, https://doi.org/10.1175/1520-0450(1992)031<0708:NPINPI>2.0.CO;2.

Mitchell, D., A. Garnier, M. Avery, and E. Erfani, 2016: CALIPSO observations of the dependence of homo- and heterogeneous ice nucleation in cirrus clouds on latitude, season and surface condition. *Atmos. Chem. Phys. Discuss.*, https://doi.org/10.5194/acp-2016-1062.

Möhler, O., and Coauthors, 2003: Experimental investigation of homogeneous freezing of sulphuric acid particles in the aerosol chamber AIDA. *Atmos. Chem. Phys.*, **3**, 211–223, https://doi.org/10.5194/acp-3-211-2003.

——, C. Linke, H. Saathoff, M. Schnaiter, R. Wagner, A. Mangold, M. Krämer, and U. Schurath, 2005: Ice nucleation on flame soot aerosol of different organic carbon content. *Meteor. Z.*, **14**, 477–484, https://doi.org/10.1127/0941-2948/2005/0055.

——, and Coauthors, 2008: The effect of organic coating on the heterogeneous ice nucleation efficiency of mineral dust aerosols. *Environ. Res. Lett.*, **3**, 025007, https://doi.org/10.1088/1748-9326/3/2/025007.

Murphy, D., K. Froyd, J. Schwarz, and J. Wilson, 2014: Observations of the chemical composition of stratospheric aerosol particles. *Quart. J. Roy. Meteor. Soc.*, **140**, 1269–1278, https://doi.org/10.1002/qj.2213.

Murray, B., D. O'Sullivan, J. Atkinson, and M. Webb, 2012: Ice nucleation by particles immersed in supercooled cloud droplets. *Chem. Soc. Rev.*, **41**, 6519–6554, https://doi.org/10.1039/c2cs35200a.

NASA, 2012: MACPEX WB-57 platform. NASA ESPO Data Archive, accessed 1 March 2016, https://espo.nasa.gov/macpex/archive/browse/macpex.

Nielsen-Gammon, J., 2011: The 2011 Texas Drought. Office of the Texas State Climatologist Rep., 43 pp.

Perring, A., J. Schwarz, R. Gao, A. Heymsfield, C. Schmitt, M. Schnaiter, and D. Fahey, 2013: Evaluation of a perpendicular inlet for airborne sampling of interstitial submicron black-carbon aerosol. *Aerosol Sci. Technol.*, **47**, 1066–1072, https://doi.org/10.1080/02786826.2013.821196.

Phillips, V., P. DeMott, and C. Andronache, 2008: An empirical parameterization of heterogeneous ice nucleation for multiple chemical species of aerosol. *J. Atmos. Sci.*, **65**, 2757–2783, https://doi.org/10.1175/2007JAS2546.1.

——, ——, ——, K. Pratt, K. Prather, R. Subramanian, and C. Twohy, 2013: Improvements to an empirical parameterization of heterogeneous ice nucleation and its comparison

with observations. *J. Atmos. Sci.*, **70**, 378–409, https://doi.org/10.1175/JAS-D-12-080.1.

Reid, J., R. Koppmann, T. Eck, and D. Eleuterio, 2005: A review of biomass burning emissions part II: Intensive physical properties of biomass burning particles. *Atmos. Chem. Phys.*, **5**, 799–825, https://doi.org/10.5194/acp-5-799-2005.

Ren, C., and A. MacKenzie, 2005: Cirrus parameterization and the role of ice nuclei. *Quart. J. Roy. Meteor. Soc.*, **131**, 1585–1605, https://doi.org/10.1256/qj.04.126.

Rieger, D., A. Steiner, V. Bachmann, P. Gasch, J. Förstner, K. Deetz, B. Vogel, and H. Vogel, 2017: Impact of the 4 April 2014 Saharan dust outbreak on the photovoltaic power generation in Germany. *Atmos. Chem. Phys.*, **17**, 13 391–13 415, https://doi.org/10.5194/acp-17-13391-2017.

Rogers, D., P. DeMott, S. Kreidenweis, and Y. Chen, 2001: A continuous-flow diffusion chamber for airborne measurements of ice nuclei. *J. Atmos. Oceanic Technol.*, **18**, 725–741, https://doi.org/10.1175/1520-0426(2001)018<0725:ACFDCF>2.0.CO;2.

Rollins, A., and Coauthors, 2014: Evaluation of UT/LS hygrometer accuracy by intercomparison during the NASA MACPEX mission. *J. Geophys. Res. Atmos.*, **119**, 1915–1935, https://doi.org/10.1002/2013JD020817.

Sargent, M. R., and Coauthors, 2013: A new direct absorption tunable diode laser spectrometer for high precision measurement of water vapor in the upper troposphere and lower stratosphere. *Rev. Sci. Instrum.*, **84**, 074102, https://doi.org/10.1063/1.4815828.

Schmitt, C., and A. Heymsfield, 2009: The size distribution and mass-weighted terminal velocity of low-latitude tropopause cirrus crystal populations. *J. Atmos. Sci.*, **66**, 2013–2028, https://doi.org/10.1175/2009JAS3004.1.

Schwarz, J., and Coauthors, 2006: Single-particle measurements of midlatitude black carbon and light-scattering aerosols from the boundary layer to the lower stratosphere. *J. Geophys. Res.*, **111**, D16207, https://doi.org/10.1029/2006JD007076.

——, and Coauthors, 2008: Measurement of the mixing state, mass, and optical size of individual black carbon particles in urban and biomass burning emissions. *Geophys. Res. Lett.*, **35**, L13810, https://doi.org/10.1029/2008GL033968.

Scott, S., T. Bui, K. Chan, and S. Bowen, 1990: The Meteorological Measurement System on the NASA ER-2 aircraft. *J. Atmos. Oceanic Technol.*, **7**, 525–540, https://doi.org/10.1175/1520-0426(1990)007<0525:TMMSOT>2.0.CO;2.

Seifert, A., and K. Beheng, 2006: A two-moment cloud microphysics parameterization for mixed-phase clouds. Part 1: Model description. *Meteor. Atmos. Phys.*, **92**, 45–66, https://doi.org/10.1007/s00703-005-0112-4.

Shi, X., X. Liu, and K. Zhang, 2015: Effect of pre-existing ice crystals on cirrus clouds and comparison between different ice nucleation parameterizations with the Community Atmosphere Model (CAM5). *Atmos. Chem. Phys.*, **15**, 1503–1520, https://doi.org/10.5194/acp-15-1503-2015.

Storelvmo, T., 2017: Aerosol effects on climate via mixed-phase and ice clouds. *Annu. Rev. Earth Planet. Sci.*, **45**, 199–222, https://doi.org/10.1146/annurev-earth-060115-012240.

Sullivan, S., R. Morales Betancourt, D. Barahona, and A. Nenes, 2016: Understanding cirrus ice crystal number variability for different heterogeneous ice nucleation spectra. *Atmos. Chem. Phys.*, **16**, 2611–2629, https://doi.org/10.5194/acp-16-2611-2016.

Thomson, D., M. Schein, and D. Murphy, 2000: Particle analysis by laser mass spectrometry WB-57F instrument overview. *Aerosol Sci. Technol.*, **33**, 153–169, https://doi.org/10.1080/027868200410903.

Ullrich, R., and Coauthors, 2017: A new ice nucleation active site parameterization for desert dust and soot. *J. Atmos. Sci.*, **74**, 699–717, https://doi.org/10.1175/JAS-D-16-0074.1.

Vali, G., P. DeMott, O. Möhler, and T. Whale, 2015: Technical note: A proposal for ice nucleation terminology. *Atmos. Chem. Phys.*, **15**, 10 263–10 270, https://doi.org/10.5194/acp-15-10263-2015.

Vogel, B., C. Hoose, H. Vogel, and C. Kottmeier, 2006: A model of dust transport applied to the Dead Sea area. *Meteor. Z.*, **15**, 611–624, https://doi.org/10.1127/0941-2948/2006/0168.

——, H. Vogel, D. Bäumer, M. Bangert, K. Lundgren, R. Rinke, and T. Stanelle, 2009: The comprehensive model system COSMO-ART—Radiative impact of aerosol on the state of the atmosphere on the regional scale. *Atmos. Chem. Phys.*, **9**, 8661–8680, https://doi.org/10.5194/acp-9-8661-2009.

Wagner, R., and Coauthors, 2012: Ice cloud processing of ultraviscous/glassy aerosol particles leads to enhanced ice nucleation ability. *Atmos. Chem. Phys.*, **12**, 8589–8610, https://doi.org/10.5194/acp-12-8589-2012.

——, J. Kaufmann, O. Möhler, H. Saathoff, M. Schnaiter, R. Ullrich, and T. Leisner, 2018: Heterogeneous ice nucleation ability of NaCl and sea salt aerosol particles at cirrus temperatures. *J. Geophys. Res. Atmos.*, **123**, 2841–2860, https://doi.org/10.1002/2017JD027864.

Walter, C., S. Freitas, C. Kottmeier, I. Kraut, D. Rieger, H. Vogel, and B. Vogel, 2016: The importance of plume rise on the concentrations and atmospheric impact of biomass burning aerosol. *Atmos. Chem. Phys.*, **16**, 9201–9219, https://doi.org/10.5194/acp-16-9201-2016.

Weinstock, E., and Coauthors, 2009: Validation of the Harvard Lyman-$\alpha$ in situ water vapor instrument: Implications for the mechanisms that control stratospheric water vapor. *J. Geophys. Res.*, **114**, D23301, https://doi.org/10.1029/2009JD012427.

Zhang, K., X. Liu, M. Wang, J. Comstock, D. Mitchell, S. Mishra, and G. Mace, 2013: Evaluating and constraining ice cloud parameterizations in CAM5 using aircraft measurements from the SPARTICUS campaign. *Atmos. Chem. Phys.*, **13**, 4963–4982, https://doi.org/10.5194/acp-13-4963-2013.